Assimilation of satellite images into a sediment transport model of Lake Michigan

Jonathan R. Stroud,[1] Barry M. Lesht,[2] David J. Schwab,[3] Dmitry Beletsky,[4] and Michael L. Stein[5]

Received 7 December 2007; revised 25 October 2008; accepted 12 December 2008; published 14 February 2009.

[1] In this paper we develop and examine several schemes for combining daily images obtained from the Sea-viewing Wide Field Spectrometer (SeaWiFS) with a two-dimensional sediment transport model of Lake Michigan. We consider two data assimilation methods, direct insertion and a kriging-based approach, and perform a forecasting study focused on a 2-month period in spring 1998 when a large storm caused substantial amounts of sediment resuspension and horizontal sediment transport in the lake. By beginning with the simplest possible forecast method and sequentially adding complexity we are able to assess the improvements offered by combining the satellite data with the numerical model. In our application, we find that data assimilation schemes that include both the data and the lake dynamics improve forecast root mean square error by 40% over purely model-based approaches and by 20% over purely data-based approaches.

Citation: Stroud, J. R., B. M. Lesht, D. J. Schwab, D. Beletsky, and M. L. Stein (2009), Assimilation of satellite images into a sediment transport model of Lake Michigan, *Water Resour. Res.*, *45*, W02419, doi:10.1029/2007WR006747.

1. Introduction

[2] Recent improvements in computer performance have led to increases in the complexity of geophysical models. Similarly, improvements in data visualization methods have led to increased emphasis on models with detailed spatial and temporal resolutions, the output of which can be presented in dramatic graphical form. Both developments in modeling have highlighted the importance of obtaining field data appropriate for evaluating and improving complex, highly resolved models. This is true particularly in the Great Lakes, because numerical models have been among the primary tools employed for understanding and assessing these systems since the 1970s, when phosphorus-induced eutrophication was the primary concern of lake managers.

[3] Current generation models are based on grid scales of O(1)-km and run on hourly or subhourly time steps, hence traditional ship-based surveys cannot collect data with either the spatial or temporal density the models need for their support. High-frequency data can be collected with instruments mounted on fixed moorings, but like ship-based surveys, these are costly unless the spatial domain of interest is small. Satellite remote sensing, which can provide information that is highly resolved in both space and time, is a promising source of data that are better matched to the models' spatial and temporal scales and that should prove most valuable for model evaluation and development.

[4] Of course, satellite methods are neither problem-free nor without serious challenges of interpretation. Some of these difficulties can be overcome by limiting the application of the observations to variables that are most directly related to the satellite measurements (e.g., surface temperature) and/or by taking advantage of temporal and spatial compositing to extract meaningful signals from inherently noisy data. Indeed, a rich body of literature has shown that valuable data can be obtained from satellite imagery, especially for studies of regional-scale and seasonal processes [*Brock and McClain*, 1992; *Uddstrom and Oien*, 1999; *Behrenfeld et al.*, 2001].

[5] Satellite observations can also be used to understand shorter-term and localized phenomena. For example, we used a 3-month time series of satellite images obtained from the Sea-viewing Wide Field Spectrometer (SeaWiFS) sensor to study a rapidly developing phytoplankton bloom in southern Lake Michigan [*Lesht et al.*, 2002]. Other researchers [*Hughes et al.*, 1998; *Kostinoy et al.*, 2004] used high-frequency imagery to study transient events in the open ocean. Relatively little work, however, has been directed toward integrating high-frequency, high-resolution imagery with high-resolution models of aquatic processes. Such integration should be useful both as a quantitative measure of the models' performance and for providing operational models with data for near-real-time assimilation [*Schwab and Bedford*, 1994].

[6] The purpose of this paper is to report on our exploration of methods for combining satellite imagery with a high-resolution numerical model. More specifically, we discuss here our integration of SeaWiFS data with a model originally developed for simulating sediment transport in Lake Michigan. Understanding and predicting the movement of suspended sediment is important in the Great Lakes, because many of the contaminants of concern in these waters are associated with fine particles, and all of the

[1]Department of Statistics, George Washington University, Washington, D. C. USA.
[2]Applied Science and Technology Directorate, Argonne National Laboratory, Argonne, Illinois USA.
[3]NOAA GLERL, Ann Arbor, Michigan USA.
[4]CILER, SNRE, University of Michigan, USA.
[5]Department of Statistics, University of Chicago, Chicago, Illinois USA.

0043-1397/09/2007WR006747

major nutrient cycles (carbon, nitrogen, phosphorus, and silicon) include significant particulate phases. The complex biogeochemical models [*Chen et al.*, 2004] being developed to assist in management of the lakes reflect this fact and depend critically on accurate representation of sediment transport processes. Even simple biogeochemical models of the Great Lakes have been shown to be most sensitive to their parameterizations of sediment transport [*Chapra*, 1977; *Lesht et al.*, 1991].

[7] Much work has been devoted to Great Lakes sediment modeling. Because data continuity has been valued more than possibly fragmented information about spatial and temporal patterns, and because time series are easier to manage than are the large three-dimensional (3-D) data sets provided by satellites, sediment model validation studies have used time series observations made at single points rather than satellite imagery. On the other hand, suspended sediments are highly reflective, and they are easily detectable in visible-wavelength satellite images. Thus, the application of satellite data to studies of sediment transport in marine and aquatic systems remains an active area of research.

[8] The first well-known exploration of satellite imagery of Lake Michigan highlighted intriguing spatial patterns indicating complex current structures [*Mortimer*, 1988] but did not attempt quantitative analyses. Other early studies in marine systems used very small sets of data for limited purposes, probably because the requirements for dealing with the satellite data exceeded the available computing capacity. For example, *Puls et al.* [1994] compared three cloud-free Coastal Zone Color Scanner images of the North Sea with a model calculation and concluded simply that their model did not successfully reproduce the observed sediment distributions. As computer memory and storage technology advanced, studies became more sophisticated and quantitative, but they still were often based on small sets of satellite images and limited model calculations [*Gerritsen et al.*, 2001; *Ransibrahmanakul and Stumpf*, 2002; *Ouillon et al.*, 2004; *Pleskachevsky et al.*, 2005]. None of these studies used satellite data either to evaluate the performance of the models as they progressed in time or to examine the effects of incorporating past data into the model to improve forecasts. These two applications are our primary focus here.

[9] In section 2 we describe the data and the numerical model, and in section 3 we discuss several concepts of forecasting and our approaches to image model integration. Our results are described in section 4. In section 5 we discuss the performance of the forecasts in some detail and illustrate how the relationships between the forecasts and observed fields provide insight valuable for improving the model and for understanding the limitations of the data. We conclude that real-time and retrospective modeling of sediment transport can be enhanced substantially by incorporating satellite imagery and that the data provided by the satellites can be important both for constraining model results and for assessing the choice of model parameter values.

2. Satellite Data and Model

2.1. Satellite Images

[10] We concentrated our analysis on a 60-day time period spanning March–April 1998, when a major sediment resuspension event occurred in southern Lake Michigan. An intensive data collection effort, known as the Episodic Events Great Lakes Experiment (EEGLE, http://www.glerl.noaa.gov/eegle/), that also began at this time is the source of the in situ data we used in this work. The resuspension event has been described in several papers resulting from the EEGLE project [*Schwab et al.*, 2000; *Eadie et al.*, 2002]. For our purposes, the points of importance are that resuspension events like the one in 1998 appear to have significant influences on lake processes, the events are easily visible in satellite images, and considerable effort has been devoted to developing models that simulate the effects of the events on the lake's biogeochemical function [*Chen et al.*, 2004].

[11] We used imagery from SeaWiFS, obtained from the Ocean Color archive of the National Aeronautics and Space Administration (NASA) Goddard Space Flight Center (http://oceancolor.gsfc.nasa.gov), in this study. We limited the data selection to overpasses between 1240 and 1440 LT and converted the level 1 images obtained from the archive to level 2 products by using NASA's SeaDAS software [*Baith et al.*, 2001]. The output products used in our analysis included remote sensing reflectance (RSR) in the eight SeaWiFS bands (six in the visible and two in the near infrared), as well as several auxiliary diagnostic variables. Our processing included an atmospheric correction [*Gordon and Wang*, 1994], a modified cloud detection and masking value (albedo at 865 nm $\geq$ 1.25%), and mapping onto a 2-km grid that was coincident with the model grid described below. For our basic analysis we further screened the images to eliminate those having fewer than 3500 cloud-free pixels among the 7347 pixels covering the southern basin. A total of 20 images, described in Table 1, passed this screening.

2.2. In Situ Data

[12] Using satellite data to retrieve the values of geophysical variables can be an involved process. The radiances received at the satellite must be corrected for the confounding effects of the atmosphere and a functional relationship must be determined between the corrected radiances and the variable of interest. Very often such relationships, or retrieval algorithms, are developed empirically. Many so-called semiempirical algorithms have been proposed for retrieving suspended sediment concentration or total suspended material (TSM) from satellite observations from a variety of sensors and bands [*Mitchelson-Jacob*, 1999]. Several groups [e.g., *Myint and Walker*, 2002; *Binding et al.*, 2003, 2005; *Budd and Warrington*, 2004; *Chen et al.*, 2004; *Warrick et al.*, 2004] have published suspended sediment algorithms specific for SeaWiFS. Using data from coastal Louisiana, *Myint and Walker* [2002] explored several statistical relationships between suspended sediment concentration and radiance in single SeaWiFS bands (555 nm and 670 nm) and determined that a quadratic model based on the 670-nm band fit the data best. In their study of suspended sediments in the Irish Sea, *Binding et al.* [2003] used similar statistical methods and also adopted a quadratic model that related reflectance (rather than radiance) at 670 nm to suspended sediment concentration. Similar work in the Great Lakes has been very limited. *Budd and Warrington* [2004] used SeaWiFS

Table 1. Summary of Satellite Remote Sensing Reflectance Values for All 20 Images Used in the Forecast Study[a]

Date	Hour	*m*	Mean	SD
		March 1998 Images		
3/12	282	5398	−3.40	0.454
3/12	283	5491	−3.36	0.392
3/16	379	4580	−3.32	0.437
3/21	498	5414	−3.53	0.420
3/22	522	6600	−3.49	0.567
3/23	546	5646	−3.45	0.544
3/23	547	6291	−3.43	0.475
3/24	570	7079	−3.52	0.592
3/26	618	4176	−3.31	0.455
3/29	691	4146	−3.33	0.463
Total		54821	−3.43	0.497
		April 1998 Images		
4/4	834	7092	−3.72	0.533
4/5	859	6601	−3.68	0.485
4/11	1003	3685	−3.54	0.528
4/12	1026	6548	−3.54	0.414
4/17	1146	6587	−3.72	0.497
4/18	1171	3563	−3.71	0.276
4/19	1194	3905	−3.61	0.437
4/23	1290	6800	−3.80	0.409
4/27	1387	3929	−3.88	0.259
4/28	1410	4633	−3.80	0.370
Total		53343	−3.70	0.453

[a]The *m* denotes number of cloud-free pixels in southern Lake Michigan; Mean and SD denote the mean and standard deviation in units of log RSR (natural logarithm of remote sensing reflectance) for the cloud-free pixels in southern Lake Michigan.

observations to derive linear relationships between suspended sediment and reflectance at 555 nm for both Lake Michigan and Lake Superior. *Chen et al.* [2004] used much of the same data set to derive two log linear relationships, one for each year of their study, predicting suspended sediment concentration as an exponential function of reflectance at 555 nm.

[13] Because the parameter estimates by *Chen et al.* [2004] varied substantially across their two study years, and because their fitted functions do not reproduce the reflectance when TSM concentrations are high, we used in situ data collected during EEGLE to develop a new function relating suspended sediment concentration to remote sensing reflectance. The locations of these EEGLE samples, along with the bathymetry of the southern basin, are shown in Figure 1. In total, EEGLE investigators made 65 near-surface TSM measurements in March and April 1998 and 1999. After a careful screening, we removed three outliers and matched the remaining 62 measurements by location and collection time with the nearest pixel of our SeaWiFS images (Figure 2). Twenty-six of the samples, were collected during our study period in 1998 and are used in our forecast evaluation.

[14] We tested several relationships between the SeaWiFS observations and TSM measurements, including those described above, and found that the following function

$$\mathrm{RSR} = 0.0027 + 0.0537 \log(1 + 0.4739\,\mathrm{TSM}), \qquad (1)$$

best represented the data, where log denotes the natural logarithm. The function is linear for small values of TSM and logarithmic at large values. Figure 2 shows a plot of the fitted function along with 62 matched TSM-RSR observations. We also use the inverse of this function

$$\mathrm{TSM} = 2.11[\exp(18.62\,\mathrm{RSR} - 0.05) - 1], \qquad (2)$$

for the data assimilation schemes described in section 3.

2.3. Sediment Transport Model

[15] Sediment transport models generally are designed to simulate the time-varying distribution of particles in the water column and sediment bed as they respond to gravitational and hydrodynamic forces. These models vary in complexity from those that yield a time series of suspended sediment concentration at a single point [*Hawley and Lesht*, 1992] to those that calculate the vertical profiles of several size classes of sediments both in the water column and the bed as they change in both space and time [*Lee et al.*, 2005]. The model we use here, which simulates the temporal and spatial evolution of the depth-averaged concentration of a single sediment class as the lake responds to wind forcing, is of intermediate complexity. Although satellite observations do not provide direct information about the vertical profile of sediment concentration our depth-averaged model is probably a good representation of the water column condition in the spring before stratification. Studies in Lake Michigan [*Hawley and Lee*, 1999; *Hawley and Muzzi*, 2003] show that the vertical distribution of material is fairly constant with depth during unstratified conditions.

[16] The hydrodynamic models used in this study include a circulation model [*Beletsky and Schwab*, 2001; *Beletsky et*

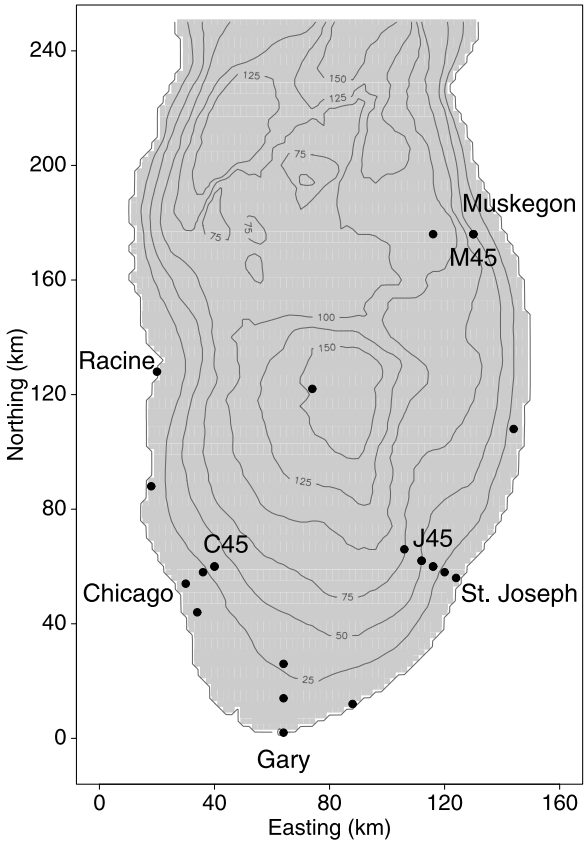

Figure 1. Southern Lake Michigan water depths and locations of the in situ measurements.

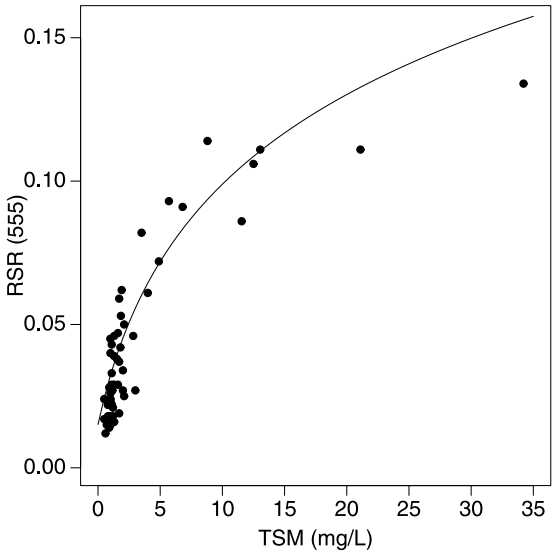

Figure 2. Matched in situ TSM measurements and satellite reflectance values, along with the RSR/TSM function defined in equation (1).

al., 2003] that is based on the 3-D Princeton Ocean Model (POM) and a surface wave model [*Schwab et al.*, 1984]. Bottom horizontal shear stress (τ) is calculated as a linear function of independent stresses resulting from the full 3-D POM (τ_{cm}) and from the wave model (τ_{wm}).

$$\tau = \left[\tau_{wm}^2 + \tau_{cm}^2\right]^{1/2}. \tag{3}$$

In our application, the horizontal flows are calculated by vertically integrating the results of the 3-D model. This is appropriate in early spring when the lake is unstratified and currents are relatively uniform with depth [*Beletsky et al.*, 2003; *Lee et al.*, 2007]. All model runs start on 1 March 1998.

[17] Several studies [*Lesht and Hawley*, 1987; *Lesht*, 1989] have shown that wave stress dominates the current stress in the Great Lakes and that the primary role of the wind-forced currents is advection of material resuspended from the bottom by the wave stress [*Schwab and Beletsky*, 2002]. Sediment resuspension is parameterized in the model in terms of excess bottom shear stress, where the threshold or critical stress is given, as are the parameters representing the sediment settling rate and resuspension rate [*Hawley and Lesht*, 1992]. Our model differs from that used by Hawley and Lesht in that it also includes the dynamics of the sediment bed, representing the quantity of sediment available for resuspension in terms of a finite bed thickness at every grid cell.

[18] Using this general framework, we write

$$\frac{\partial(dc)}{\partial t} = -u\frac{\partial(dc)}{\partial x} - v\frac{\partial(dc)}{\partial y} + s, \tag{4}$$

$$\frac{\partial b}{\partial t} = -\frac{s}{\rho}, \tag{5}$$

where $c \equiv c(x, y, t)$ is the vertically averaged sediment concentration at location (x, y) and time t, $d \equiv d(x, y)$ is the water depth, $b \equiv b(x, y, t)$ is the sediment bed thickness, $u \equiv u(x, y, t)$ and $v \equiv v(x, y, t)$ are the water velocities, $s \equiv s(x, y, t)$ is the vertical flux which incorporates resuspension and settling, and ρ is the bulk bed sediment density which we assume is 2.5 (g/cm^3) [*Krone*, 1962; *Partheniades*, 1962].

[19] We assume bed-limited resuspension, so that $s = \min(s^*, \kappa b)$, where κ is the sediment density-based factor relating the sediment mass flux to the change in bed thickness [*Lee et al.*, 2005] and s^* is the vertical flux for a bed of unlimited thickness, which is defined as

$$\begin{aligned} s^* &= -w_s c + \epsilon\left(\frac{\tau}{\tau_c} - 1\right), \quad \text{if } \tau \geq \tau_c, \\ s^* &= -w_s c, \quad \text{if } \tau < \tau_c. \end{aligned} \tag{6}$$

Here $\tau = \tau(x, y, t)$ is the bottom shear stress, w_s is the settling velocity, τ_c is the critical bottom shear stress and ϵ is the resuspension rate. We implemented this model on a 2-km grid of Lake Michigan consisting of 131 rows and 251 columns and a total of 14,458 water cells. The model initial conditions and parameter values are listed in Table 2. The values were chosen to represent the sediment grain size and properties typical of the southern basin of the lake [*Lee et al.*, 2005] and to minimize forecast errors with respect to the satellite data, as described in section 4.

3. Methods

[20] We consider the following forecasting problem: Given an initial condition, expressed here as the assumed spatial distribution of TSM on the 2-km grid on 1 March 1998, how do we best predict the evolution of the RSR field in time? Because we are concerned with the relative accuracy of our forecasts, we present most of our results in terms of the transformed variable log RSR, and we emphasize relative rather than absolute errors. We conducted similar analyses using several response variables, including TSM and RSR, and determined that this transformation does not materially affect the results (see Table 3).

[21] Of course, forecasting methods vary considerably in complexity. Although we assumed that the best forecasting technique would involve application of a physically based numerical model driven by specified time series observations of external forcing mechanisms, we also considered forecast methods that do not include lake dynamics. Our ultimate goal, again, is to determine the extent to which concurrent observations of the state of the system, provided by satellite measurements, can improve the accuracy of the resultant forecasts. By using the satellite images for com-

Table 2. Initial Conditions and Parameter Values for the Sediment Transport Model

Parameter	Symbol	Value
Initial bed	b_0	2 mm
Initial TSM	c_0	0.01 mg/L
Settling rate	w_s	3.5×10^{-5} m/s
Resuspension rate	ϵ	0.05 kg/m^2/s
Critical shear stress	τ_c	0.10 N/m^2

Table 3. Summary of the One-Image-Ahead Forecast Bias and Root Mean Square Error for the Satellite and in Situ Data[a]

	Satellite Data						In Situ	
	Log RSR		RSR (%)		TSM		TSM	
Forecast Method	Bias	RMSE	Bias	RMSE	Bias	RMSE	Bias	RMSE
Base case	0.346	0.489	1.10	1.97	1.08	2.85	4.75	9.73
Persistence	−0.022	0.299	−0.07	1.37	−0.07	2.43	1.74	9.07
Pure model	0.076	0.409	0.17	1.67	0.20	2.57	1.42	7.70
Direct insertion	−0.018	0.236	0.00	1.04	0.11	1.87	1.66	6.17
Kriging	−0.023	0.234	−0.02	1.02	0.09	1.84	1.61	6.04
Observed[b]	−3.570	0.496	3.28	2.30	2.11	3.31	7.89	9.60

[a]RMSE, root-mean-square error.
[b]The mean (bias) and standard deviation (RMSE) for the observed data.

parison with the forecasts, we can both explore and quantify the attributes of the various forecast methods. Note that we distinguish here between forecasting, in which we use the model and past data to predict a future state of the system, and smoothing, in which we might look ahead in time and retrospectively adjust the model trajectory to match a known future state.

3.1. Base Case

[22] In order to establish a base case with which to compare our more complex forecasting methods, we consider a forecast which assumes that the lake has spatial variation but does not evolve in time. To obtain a valid out-of-sample forecast with similar characteristics as our study period, we constructed this field using satellite data from March and April 1999 and 2000, the 2 years following the study period. We defined the base case forecast field as the average of the satellite log RSR at each pixel across the 61 available images during this 4-month period. This field was used as the ''Base Case'' forecast for each of the 20 satellite images during the March–April 1998 study period.

3.2. Persistence

[23] We also consider a persistence approach which does not incorporate lake or sediment dynamics but updates the field using available data at each image time. Here, the forecast is initialized to the base case field, and is then is updated at each subsequent image using observed satellite data. Specifically, at each image time during the modeling period, we reset the forecast at the cloud-free locations to the observed satellite values, and leave the forecasts at the cloud-covered locations unchanged. Comparison of the persistence forecasts to the data assimilation forecasts described in section 3.4 allows us to quantify the impact of incorporating model dynamics.

3.3. Pure Numerical Model

[24] We also calculated forecasts based entirely on the sediment transport model (see section 2.3) without data updating. This scheme provides a control case against which to compare the data assimilation schemes described below, and allows us to quantify the incremental impact of incorporating data into the forecast. For the pure model forecasts, we ran the model forward from fixed initial conditions (see Table 2), forcing it with the meteorological wind fields interpolated from observations [see *Beletsky et al.*, 2003]. The model is run on an hourly external time step over the 2-month period (1 March to 30 April 2008). At each image time, the forecast errors are computed as the difference between the observed satellite data and the modeled fields at that time.

3.4. Data Assimilation

[25] The forecasting methods described above rely on either the physical model or the satellite data, but not both. By combining these two sources of information, we might hope for a substantial reduction in forecast error, though this is not necessarily the case. If both the model and data were badly in error, combining them would merely confound the problems. Adding bad data to a good model would diminish the value of the model; similarly, using a bad model with good data still would yield unreliable forecasts. Many methods have been developed for combining models and data, though often without recognition of the implicit assumption that both model and data provide some reasonable representation of the system of interest. Generally known as data assimilation [*Kalnay*, 2003], the methods are intended to capture the best of both approaches, though implementation varies considerably from application to application.

[26] We consider two data assimilation schemes which sequentially incorporate observations into the model in a conceptually simple manner. At the initial time (1 March 1998) the model state variables (TSM and bed thickness) are set to the spatially constant values given in Table 2. The sediment transport model is then run forward with the prescribed meteorological forcing until the first image time (282 h after initialization). We use equations (1) and (2) to convert between TSM and log RSR. Subsequently, we repeat the following steps for each image:

1. Convert the modeled TSM field to log RSR.
2. Compute the forecast error (data minus forecast).
3. Update the modeled log RSR field.
4. Convert the updated log RSR field back to TSM.
5. Run the sediment model forward to the next image time.

[27] This algorithm provides a sequence of one-image-ahead forecasts. The one-image-ahead error field is calculated from the differences between each image and the corresponding forecast. We also determined k-image-ahead forecast errors by running the model with updates to image i and then running ahead without updates to the end of the T image series, calculating the forecast error at every image $i + k$ for $1 \leq k \leq T - i$.

[28] We would expect that in the absence of updating the forecast trajectory would diverge from the observations as a function of the length of time between updates. The average time interval between satellite updates was 2.4 days, with a range of 1 h (two successive satellite passes) to 6 days. We did calculate the errors for the k-image-ahead forecasts and found that in terms of the relative success of the different assimilation methods, they did not differ substantially from the one-image-ahead forecasts. We report only the one-image-ahead results here.

[29] Note that the number of pixels included in the forecast error calculation (step 2) depends on the completeness of the image and that our image screening guaranteed that at least 3500 pixels were used. Also note that to minimize the potential effect of model spin-up time on the comparison among forecast methods we did not use the first image (hour 282) in the error analysis. Because the satellite

images do not directly inform us about changes in the sediment bed, we do not update the sediment bed thickness at step 3. Long-term mass conservation is not required by the assimilation model, however, because in reality new sediment is introduced into the lake by shoreline erosion and direct deposition during the course of the year. Because the sediment model includes gravitational settling, some of the changes in the calculated suspended sediment mass introduced by the updating eventually result in changes in the bed thickness. We do track sediment mass during the modeling process and the degree to which our calculations deviate from mass conservation is described in section 5.

[30] We focus here on the results obtained from two update schemes: direct insertion and kriging. Certainly, many other assimilation schemes are in common use [see *Kalnay*, 2003], but these two depend only on past data and are appropriate in the pure forecasting mode that we are testing.

3.4.1. Direct Insertion

[31] Direct insertion is a simple approach for satellite data assimilation in which the satellite data are ''inserted'' into the forecast model at each observation time. Specifically, at each image time, the forecast at each observation location is replaced with the satellite data value at the corresponding location; the forecasts at cloud-covered pixels are left unchanged. The direct insertion approach provided a computationally fast updating scheme, since only one observation is used to update the forecast at each pixel, implying a cost which is linear in the number of observations. However, this approach may lead to discontinuities in the updated field due to the lack of spatial smoothing around the edge of the cloud cover. This can be especially problematic if there is a large mismatch between the satellite data and the forecast. We note that the persistence approach (section 3.2) is equivalent to the direct insertion approach without the lake or sediment dynamics.

3.4.2. Kriging

[32] To avoid spatial discontinuities in the updated fields, it may be desirable to update the entire forecast field rather than at just the cloud-free locations. Kriging-based approaches [*Cressie*, 1993] provide a method for spatial interpolation that is optimal if the covariance model is correctly specified. The covariance function may be chosen on the basis of analysis of the data fields or may be prespecified, depending on the application. Given a set of data and a covariance function, the so-called kriged estimates are the best linear, unbiased estimates of the unknown field at all locations.

[33] We assume the following observation model at each image time:

$$\mathbf{y}^o = \mathbf{H}\mathbf{y}^f + \mathbf{e}, \tag{7}$$

where $\mathbf{y}^o$ is the $m \times 1$ satellite observation vector, $\mathbf{y}^f$ is the $n \times 1$ model forecast vector, $\mathbf{e}$ is the $m \times 1$ forecast error vector (all expressed in units of log RSR), and $\mathbf{H}$ is an $m \times n$ incidence matrix with jth row given by $\mathbf{H}_j = (0, \ldots, 0, 1, 0, \ldots, 0)'$, where the position of the 1 matches the jth observation to a component of the forecast vector.

[34] In Equation (7), the errors $\mathbf{e}$ represent all sources of uncertainty, including those in the physical model, in the satellite retrieval function, and in the atmospheric correction algorithm. To account for the spatial correlations in these sources, we model $\mathbf{e}$ as a realization from a stationary Gaussian random field with constant mean and covariance function $C(d) = \mathrm{cov}[e(\mathbf{s}), e(\mathbf{s}')]$, where $e(\mathbf{s})$ denotes the error at locations $\mathbf{s}$, and $d = \|\mathbf{s} - \mathbf{s}'\|$ is the Euclidean distance between $\mathbf{s}$ and $\mathbf{s}'$.

[35] For the analysis presented in section 4, we assume that the errors have mean zero (i.e., the forecasts are unbiased estimates of the data), and the following covariance function:

$$C(d) = \sigma^2 \exp(-d/\lambda)\, k_r(d). \tag{8}$$

Here σ^2 represents the variance parameter; λ is the spatial range parameter; r is the spatial cutoff distance; and $k_r(d)$ is the fifth-order polynomial correlation function of *Gaspari and Cohn* [1999, equation 4.10], which is zero for all distances $d > r$. In our analysis, we choose r to be small, implying zero correlation for most pairs of grid points. This greatly reduces the computational cost of the update step, as described below. The covariance model (8) was chosen after considering other more complicated covariance functions, including members of the Matèrn family [*Stein*, 1999], nonstationary and anisotropic covariance functions, and those with a nugget effect. However, we found that these more complicated models did not substantially improve the forecast performance.

[36] Let $\mathbf{\Sigma}$ denote the $n \times n$ error covariance matrix defined at the model grid points; i.e., $\Sigma_{ij} = C(d_{ij}; \theta)$, where $d_{ij} = \|\mathbf{s}_i - \mathbf{s}_j\|$ denotes the distance between model grid points $\mathbf{s}_i$ and $\mathbf{s}_j$. The updated log RSR field, $\mathbf{y}^u$, is then obtained through the kriging equation:

$$\mathbf{y}^u = \mathbf{y}^f + \mathbf{K}\mathbf{e}, \tag{9}$$

where $\mathbf{K} = \mathbf{\Sigma}\mathbf{H}'(\mathbf{H}\mathbf{\Sigma}\mathbf{H}')^{-1}$ is the $n \times m$ matrix of kriging weights. Direct implementation of the kriging equation involves solving an $m \times m$ linear system, which requires $O(m^3)$ operations. Since m is prohibitively large in our application ($m > 3500$), we use an efficient variational approach to solve the system (see Appendix A). Under our assumption of no measurement error, the kriged estimates $\mathbf{y}^u$ match the observations $\mathbf{y}^o$ at the cloud-free locations and provide spatial smoothing near the edge of clouds. The amount of smoothing is controlled by the range parameter λ, with large values of λ providing more smoothing and small values providing less smoothing. In the limit as $\lambda \to 0$, no spatial smoothing is used, and the kriging and direct insertion approaches yield identical results.

4. Results

[37] We applied the forecasting methods described above to SeaWiFS data collected in March–April 1998. As noted above, this time period included a major resuspension event in southern Lake Michigan. Strong (20 m/s) north winds blowing along the long axis of the lake for several days in early March 1998 generated waves at the south end of the lake that exceeded 6 m in height. When the storm passed and the sky cleared on March 12, satellite images showed a region of high reflectance, interpreted as newly resuspended and eroded sediments, extending along the entire southern

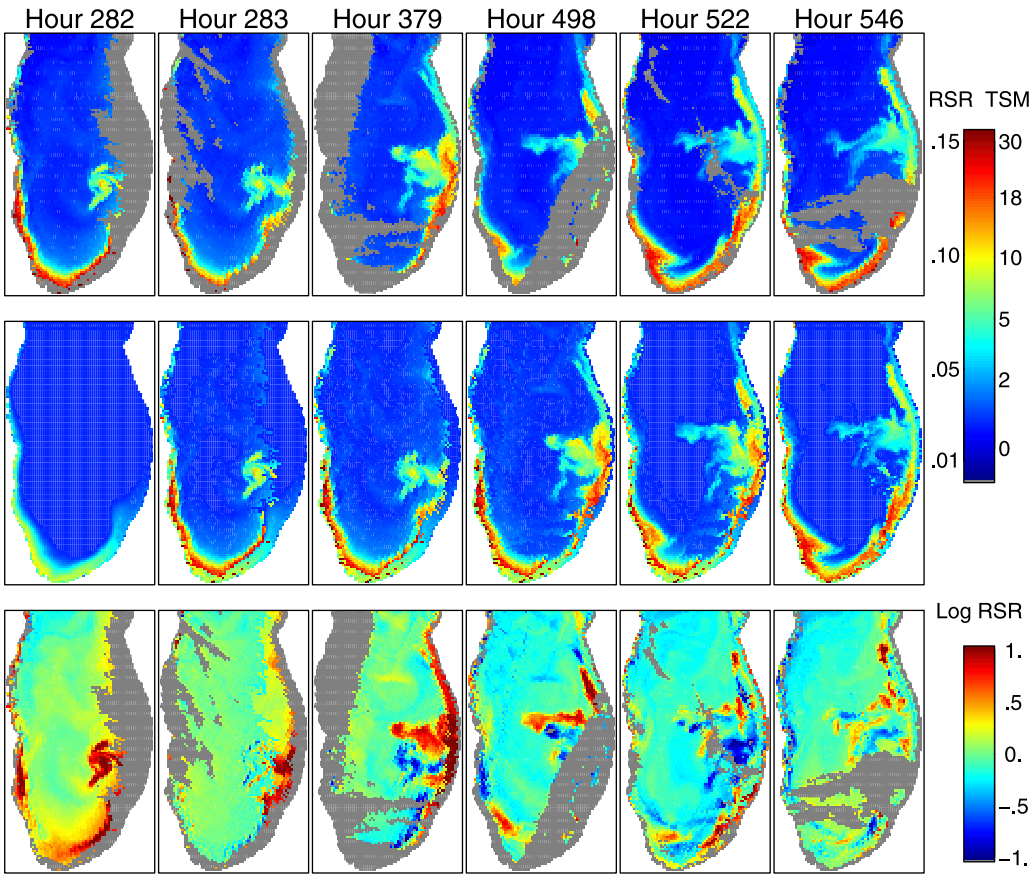

Figure 3. Satellite data and one-image-ahead persistence forecasts at the first six image times. (top) Satellite data; (middle) persistence forecasts; (bottom) forecast errors (data minus forecasts). Gray pixels indicate cloud cover.

coastline of the lake (approximately 300 km). Subsequent satellite images collected over the next several weeks showed both along- and cross-shore transport of the suspended sediment, corresponding to the general counterclockwise circulation pattern in this part of Lake Michigan [*Beletsky et al.*, 1999]. Other smaller events later in March and in early April added to the sediment burden, especially near the shore. By the middle of April, the water column was almost clear of suspended sediment, and the minimum RSR values were at or below 1% for the rest of the month, especially in the offshore area.

[38] In the ideal case, the forecasts would perfectly match the data at each point in space and time. In practice, of course, we must consider the effects of systematic errors in both the model and data, as well as random errors that might result from factors like poor or inconsistent registration of the satellite images or misspecification of the TSM-RSR functional relationship. We characterized the results of the forecasting methods statistically in terms of bias and root-mean-square error (RMSE). Let Y_{tj} denote the observed satellite or in situ data at time t and location j, $\hat{Y}_{tj}$ the corresponding predicted value, and N the number of observations used to compute the statistic. We consider the error statistics

$$\text{Bias} = \frac{1}{N}\sum_{t,j}\left(Y_{tj} - \hat{Y}_{tj}\right) \text{ and RMSE} = \sqrt{\frac{1}{N}\sum_{t,j}\left(Y_{tj} - \hat{Y}_{tj}\right)^2}.$$

Table 3 summarizes these statistics for the one-image-ahead forecasts.

4.1. Base Case

[39] The error statistics listed in Table 3 show that the base case forecast performs poorly. The RMSE across the 19 images is only slightly smaller than the overall standard deviation of the observations for log RSR, and it is larger than the RMSE values for the other forecast methods tested. When compared with the 62 in situ samples (Table 2), the base case forecasts are more variable, and their mean is 60% below the observed mean. The problem with the base case forecast is illustrated in Figure 3, which shows the results obtained by using the persistence method (presented in more detail below). Figure 3 (top) shows the first six satellite images in our data series. Figure 3 (middle) shows the forecast fields at each image time, and Figure 3 (bottom) shows the differences between the two. Because the persistence method does not include lake or sediment dynamics, the first forecast shown (Figure 3, middle, hour 282) is simply the base case mean from the 1999–2000 data. Even though the base case field shows increased sediment concentrations near the coasts in the southern basin due to spring resuspension events that occurred in 1999 and 2000, the sediment concentrations are much lower than those observed in 1998. As a result, the errors in the first forecast (Figure 3, bottom, hour 282) are substantial. Because the base case forecast is constant in time, the same forecast field (Figure 3, middle, hour 282) is used for every one of the

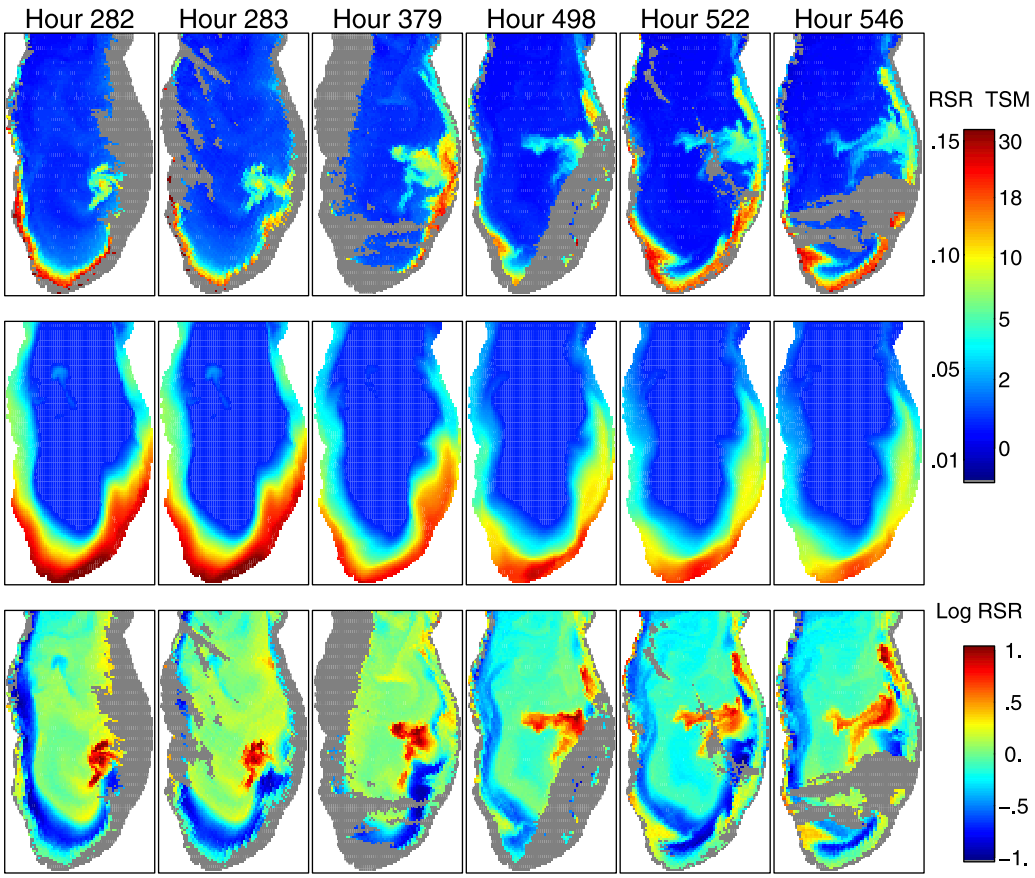

Figure 4. Satellite data and pure model forecasts at the first six image times. (top) Satellite data; (middle) model forecasts; (bottom) forecast errors (data minus forecasts). Gray pixels indicate cloud cover.

subsequent images. Only when the high sediment concentrations associated with the March 1998 event are reduced by settling and advection do the errors associated with the base case forecast fall to levels near zero.

4.2. Persistence

[40] The persistence method, which incorporates the satellite data without lake or sediment dynamics, substantially reduces the forecast errors from the base case values. Table 3 shows that the persistence forecast RMSE for satellite log RSR is approximately 40% lower than for the base case. However, with respect to the in situ data, the persistence method shows only a slight improvement from the base case. Figure 3 shows that the updated forecasts (e.g., Figure 3, middle, hour 283) are calculated by replacing the forecast values (Figure 3, middle, hour 282) with the available data (Figure 3, top, hour 282). The magnitude of the errors depends on the time interval between the observations and the completeness of the data set used for updating. Examination of the errors in Figure 3 (bottom) shows, for example, that because much of the east coast of the lake was cloud covered at hour 282, the forecast for hour 283 (next available image) assigned the base case values (Figure 3, middle, hour 282) to these pixels. Because fewer pixels along the east coast were cloud covered at hour 283 and also had log RSR values higher than the corresponding forecast values, the errors along the east coast are large and positive (Figure 3, bottom, hour 283).

[41] The importance of including lake dynamics in the forecasts is clearly shown by the persistence forecast errors at hour 379 in Figure 3 (bottom, hour 379). In the 96 h between the second and third observations, the highly reflective area on the eastern side of the lake has both changed shape and moved north. Because the persistence forecast does not include dynamics, it cannot represent this movement, and the error image shows a positive error at the new location of the reflective area and a negative error at its previous location. We note that such negatively correlated errors may cancel out when images are averaged over time, which suggests a possible limitation of model-satellite comparisons that are based solely on the long-term statistical distributions of state variables. We avoid this limitation with the image-by-image analysis reported here.

4.3. Pure Numerical Model

[42] Figure 4 shows the forecast results obtained by using the pure model. These parameters are optimized in the sense that they were selected to minimize the RMSE between the direct insertion forecasts and our observations. They fall within the range of similar parameters used by others modeling sediment transport in the Great Lakes [*Hawley and Lesht*, 1992; *Cardenas et al.*, 2005; *Lee et al.*, 2005] Although the model was initialized to spatially constant conditions and is based on the spatially uniform and nominal (though realistic) sediment transport parameters listed in Table 2, it reasonably reproduces the general

sediment concentration patterns we see in the observations. In particular, the pure model does very well at representing the long, narrow band of sediment running up the east coast and also suggests the westward offshore transport of sediment seen in the images at hours 522 and 546.

[43] This apparent qualitative success is not reflected in the error statistics (Table 3), however. Though it performed better than the base case forecast, the overall errors associated with the pure model forecast are positively biased and have substantially larger RMSE, for all the response variables, than those for the persistence forecast. Much of the error results from the tendency of the pure model to predict wider bands of suspended sediment along the coasts, as well as its understandable failure to simulate the large localized area of high reflectance that appears in the first image and dominates many of the subsequent scenes. The fact that the pure model tends to spread the sediment band beyond the limits suggested by the data also is reflected in the in situ sample statistics; the high bias results from the prediction of lower values than are observed, and the lower RMSE indicates that the forecast errors are smaller than those for the base case and persistence forecasts. Some of these problems might be alleviated by incorporating a more complex sediment resuspension model, introducing spatial dependence of the sediment model parameters, or by improvements in the hydrodynamic circulation model.

4.4. Assimilation: Direct Insertion and Kriging

[44] The primary difference between the two assimilation methods used in this study is that kriging allows us to update the entire field at each image time, rather than limiting the update to the possibly discontinuous set of available pixels used in direct insertion. As noted above, the two methods are equivalent in the limit as the spatial range parameter λ in equation (8) goes to zero. Although the two methods differ conceptually, their forecast error statistics presented in Table 3 are very similar and we discuss them together. Both reduce the RMSE in satellite log RSR by approximately 50% relative to the base case forecast and approximately 40% when compared to the pure model.

[45] One of the goals of data assimilation is to adjust the model forecasts to agree better with new observations and provide more accurate predictions going forward. We would expect, for example, that the model's tendency to predict wider sediment bands than are observed along the coasts would be mitigated when the forecasts are adjusted to reflect the narrower features typical of the data. Similarly, the problem associated with the model's failure to simulate the localized offshore area of high sediment concentration that appeared on March 12 would be resolved in the subsequent forecasts by the insertion of the March 12 observations during the update step.

[46] The additional step (analysis of the image field being used for update) required for the kriging method is illustrated in Figure 5. Rather than update the forecasts (Figure 5, middle) with the data (Figure 5, top) at only those pixels for which we have data, as would be the case for direct insertion, under the kriging method we first use equation (9) to create an analyzed field. The analyzed field is then run forward using the numerical model to obtain the forecast for the next image (e.g., Figure 5 (middle, hour 379) is the forecast based on the updated field at the second image time). Note that since our covariance model assumes no measurement error, the direct insertion and kriging updates are the same at the cloud-free pixels. This point is important for understanding why the direct insertion and kriging results are so similar for these data.

5. Discussion

5.1. Model Decomposition

[47] One goal of our analysis was to use the time series of high-resolution satellite images to validate the performance of the sediment transport model. This type of model-data comparison is useful for gaining insight into how well the important physical processes are represented in the model. One way to examine model performance is to isolate the processes represented in the model and determine how they influence the model's forecasting ability. Table 4 shows the results of such an experiment, in which we used direct insertion assimilation to test each of the eight possible combinations of the three model components (advection, resuspension and settling). This was done by running the model eight times with the separate processes turned off and on sequentially. Note that the "none" values in Table 4 correspond to the persistence results, since the persistence method is equivalent to direct insertion with all physical processes turned off.

[48] Adding the resuspension process alone slightly reduces the variability of the forecast errors but increases the bias. The positive bias values are due to the addition of sediment to the water column by the resuspension process without a compensating loss mechanism. When settling is included in the model, the bias is reduced to near zero, and the variability of the errors is reduced further, suggesting that the settling and resuspension parameter values listed in Table 2 are within a reasonable range. The converse situation, when settling is added alone, is highly biased but in the opposite direction. The positive bias reflects the steady loss of material from the water column by settling between update steps. As would be expected, this bias, though still positive, is reduced substantially when advection is added to the settling. The error variability, however, is not much different from that for the case when settling and resuspension are included without advection.

[49] The error variability is reduced substantially when advection is combined with resuspension, indicating the dominant role that local resuspension plays in accounting for the variability in the observations. The large bias, of course, is again the result of adding material without providing for a counterbalancing loss mechanism. Both the bias and RMSE are reduced to their final values when settling is added in the complete model.

5.2. Parameter Estimation

[50] We could, in principle, use the bias and RMSE calculations to adjust the sediment model parameters to some set of optimal values. Indeed, as described above, we optimized our parameter estimates to minimize the direct insertion RMSE to obtain the parameter set listed in Table 2. To be most useful, however, we also would have had to include a spatial variation in all of these parameters, something that is of great interest, but that we were not prepared to pursue in this study. Our aim was to explore assimilation methods rather than to perform a model calibration exercise [*Lee et al.*, 2005], so adding spatial

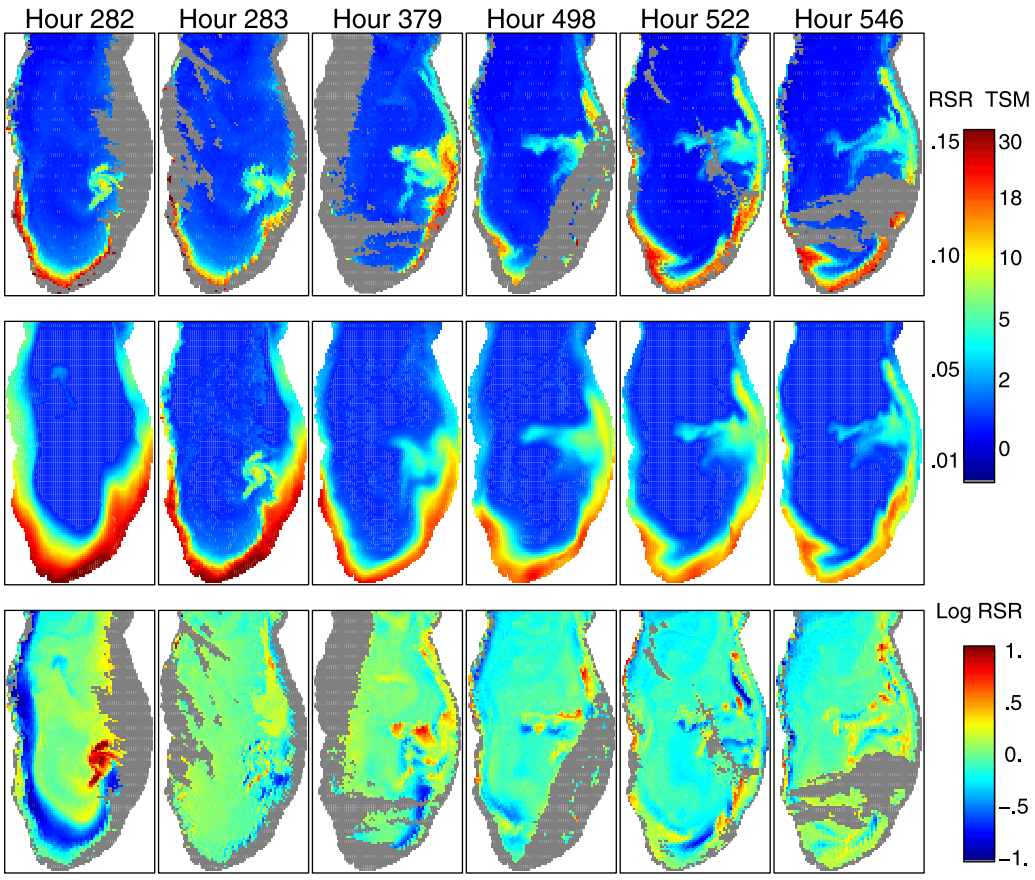

Figure 5. Satellite data and one-image-ahead kriging forecasts at the first six image times. (top) Satellite data; (middle) kriging forecasts; (bottom) forecast errors (data minus forecasts). Gray pixels indicate cloud cover.

variability to the parameter values remains a problem for future work.

5.3. Coastal Analysis

[51] Analysis based on the whole basin results allows us to assess the overall performance of the model. Others have commented on the steep gradient in reflectance associated with the edge of the nearshore resuspension feature, which generally is about 10 km wide [*Eadie et al.*, 1996; *Rao et al.*, 2002]. Therefore, evaluation of the model's ability to reproduce this feature is also of interest. We find that the pure model tends to predict wider (∼25 km) nearshore zones of high reflectance and smaller gradients than are seen in the satellite data.

[52] Figure 6 shows the model and assimilation forecasts near the coasts, along with data obtained by satellite and from EEGLE. The EEGLE data include both in situ samples and TSM measurements obtained from a phytoplankton survey system (PSS). This system, described by *Liebig et al.* [2006], consists of a sensor package that changes depth as it is towed through the water at a relatively slow speed. The PSS thus provides a nearly continuous measure of the sampled variables through the water column for the length of the transect. The sensor package includes an optical particle counter that measures bulk light attenuation values. These are converted to TSM using the method described by [*Winkleman et al.*, 1998]. Figure 6 shows the pure model and assimilation forecasts for an hour within the PSS sampling period (St. Joseph and Muskegon transects) or the time period required to collect the grab samples (Chicago transect), the PSS data (St. Joseph and Muskegon), and the satellite data nearest in time to the other data. The satellite data are displayed both as values along the transect and as excerpts from the images that include the transects. In the case of the Chicago transect, the nearest satellite data follow the water column observations by about 3 days. For the Muskegon transect, satellite images were available about 3 days on either side of the PSS data. Along the St. Joseph transect, the nearest satellite data precede the model forecasts and other observations by about 4 h. The image

Table 4. Summary of the One-Image-Ahead Forecast Bias and RMSE for the Direct Insertion Approach With Different Combinations of the Sediment Model Components[a]

Model Components	Bias	RMSE
None	−0.022	0.299
Settling	0.059	0.360
Resupension	−0.035	0.295
Settling, resuspension	0.001	0.285
Advection	−0.037	0.277
Advection, settling	0.039	0.294
Advection, resuspension	−0.063	0.256
Advection, settling, resuspension	−0.018	0.236

[a]RMSE is in log RSR units. Sediment model components are advection, settling, and resuspension.

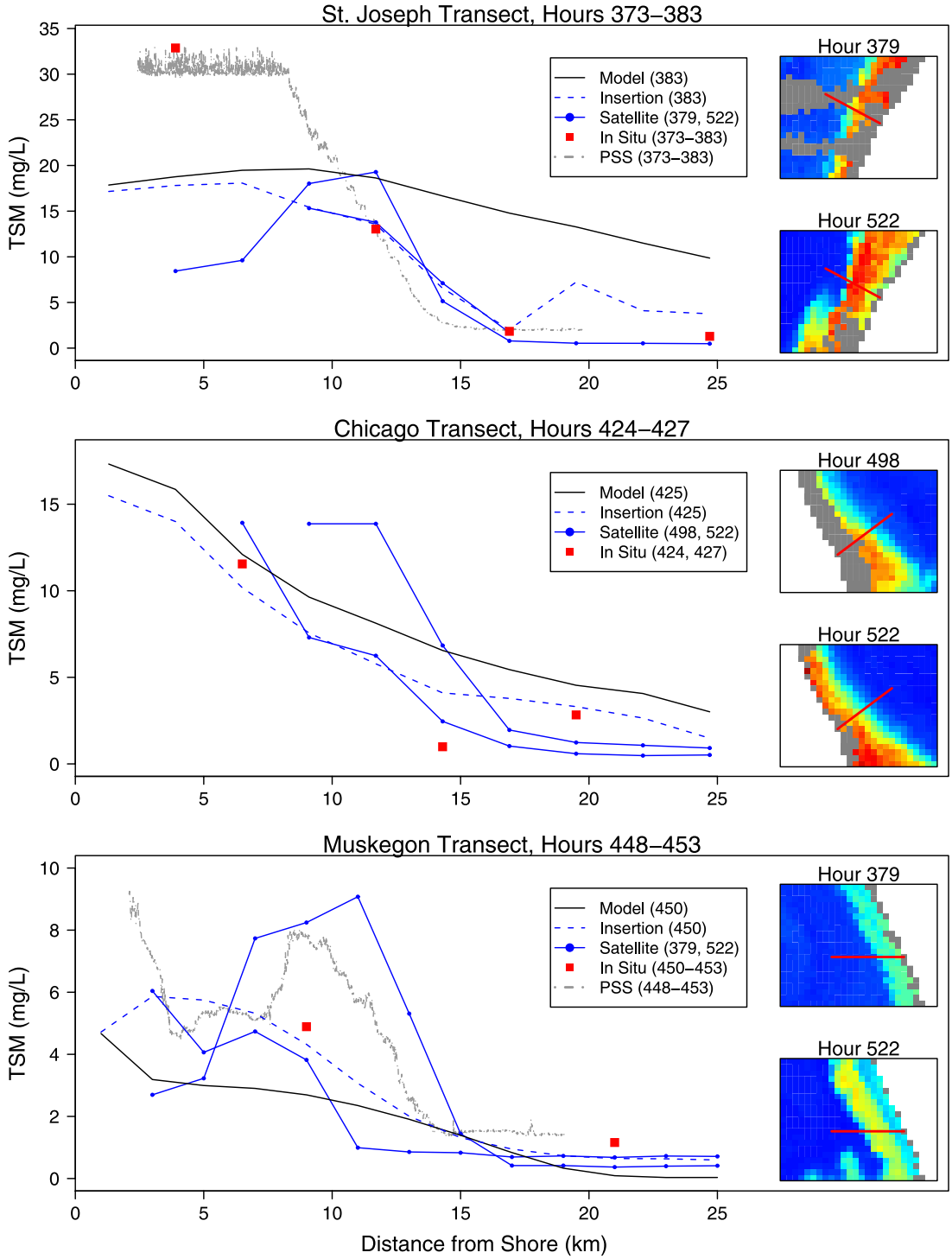

Figure 6. Forecast results for the pure model and direct insertion approaches for three transects in southern Lake Michigan. Satellite data, in situ data, and phytoplankton survey system (PSS) data during the same time period are also shown. The inset plots are the satellite images at the closest two image times, and the transect locations are indicated by line segments.

collected at hour 522 was clear for all three transects. To illustrate the evolution of the nearshore features, we also show the hour 522 satellite data with the St. Joseph and Chicago transects.

[53] The flatness of the pure model forecasts near the coasts is evident in all the transects shown in Figure 6. The assimilated forecasts are steeper, though they do not generally equal the gradients seen in the data. The satellite values agree well with the in situ samples and PSS values, though one has to view this agreement carefully, because both the PSS and satellite data were calibrated with data from the same set of in situ samples. The agreement between the satellite

data and insertion forecast at St. Joseph reflects the fact that the satellite data were incorporated into the forecast at hour 379. In this particular example the major differences between the insertion and model forecasts are seen in the region more than 10 km offshore. The TSM values estimated by the insertion forecast drop steeply and match the grab sample and PSS values, but the pure model forecast remains relatively constant, underestimating the observed gradient. A similar situation is seen in the Muskegon transect, where both the satellite data and PSS indicate a sharp drop-off in TSM beyond 10 km. Although the steep gradient is not so clear in the insertion forecast, we must consider that this forecast was last updated at hour 379, about 3 days before the PSS and grab sample collection and about 5 days before the next image. During that time, the insertion forecast will tend to move toward the pure model upon which it is based.

5.4. Kriging Versus Direct Insertion

[54] We had expected that kriging would improve upon direct insertion by smoothing the forecast fields in a way that captured the observed covariance of the observations. Our results, however, show that kriging reduces the forecast errors only minimally. One reason for this is that we assumed no measurement error so that the updated fields for direct insertion and kriging are identical at the cloud-free pixels. Also, as noted above, we used a small spatial range parameter of $\lambda = 2$ for the kriging approach, implying that only forecasts within a few pixels of cloud-free data are modified in the update step. Although we experimented with different covariance models, including ones that were locally anisotropic, none substantially improved the forecast results. This is a consequence of our assumption that the forecast errors are unbiased (i.e., have mean zero). Thus, kriging would tend to underpredict higher values in coastal regions, where cloud cover often obscures the images. We also found that using an error model that included a constant bias did not reduce the forecast error. Conceivably, one could construct a more complex model error function for use in an anisotropic and adaptive kriging procedure, but such an effort is beyond the scope of this paper.

[55] One of the challenges associated with using satellite data is that the images are often incomplete and fragmented. Although our initial screening was intended to ensure that we began with fairly complete images, our results will be affected by discontinuities introduced by cloud boundaries and retrieval failures. Each of our assimilation methods produces a complete field at the update step. In the case of direct insertion, obscured or missing pixels are set to their last forecast value, which may be quite different from the value in a neighboring good pixel. Although kriging replaces the obscured pixel value with a weighted function of the nearby good observations, discontinuities in the updated fields are reduced only slightly, because the range parameter (λ) is small. Unfortunately, the prevailing southwesterly winds over southern Lake Michigan tend to result in formation of cumulus clouds over the eastern shoreline. Thus, this region, which also tends to have the highest variability in TSM, is more often obscured than other regions, and the errors in the gradient forecasts along the eastern shore are increased as a result.

5.5. Time Series Analysis

[56] The performance of the assimilation can be assessed by comparing time series of the forecasts obtained by using the pure model and direct insertion approaches. Figure 7 shows these results for three nearshore stations located along the Chicago, St. Joseph and Muskegon transects (C45, J45 and M45; see Figure 1) along with the satellite and in situ data at those locations. For reference, the wind speed and direction in the center of the northern basin are shown in Figure 8. The assimilation forecasts diverge from the pure model forecasts after the first update at hour 282. Note that the assimilation forecasts are not nudged toward the observations but are obtained by running the model forward from the update time with only the initial conditions modified by the assimilated data. We see, for example, that at station J45 the assimilation at hour 379 requires the water column concentration to be reduced substantially. This relatively low concentration is confirmed by the grab sample collected at hour 376 and by the subsequent satellite observation. After hour 522 the assimilation model forecasts a rapidly increasing sediment concentration, which again is confirmed by the satellite observation at hour 570. The pure model also forecasts an increase in concentration during this time period, but one of much lower magnitude. Finally, the pure model and assimilation forecast converge late in the record, after a prolonged period with little or no sediment resuspension.

[57] The results shown in Figure 7 and Table 4 provide insight into both the importance of the various modeled processes and the values of the model parameters. Because we have not adjusted the model parameters, both the pure model and assimilation forecasts respond in the same ways to the forcing shear stress. The advective flows are also the same in both forecast schemes. Thus, differences between the two forecasts must result from differences in the amount of available sediment and the suspended sediment concentration fields that are advected between pixels. The results in Table 4 show that advection is the single most important process for reducing the forecast error of the model. We already have noted the tendency of the model to transport too much material offshore. The difference in the forecast at Station J45, for example, occurs because the assimilation scheme keeps more material inshore and available for northward advection.

[58] We noted that our assimilation methods do not conserve mass. Depending on the retrieved sediment concentrations used in the update step suspended mass may be added or removed from the system. However, mass conservation is not required in the filtering application we describe here where our goal is to provide the best forecast going forward from the point at which the modeled field is updated with new data. We also noted that in the assimilation we do not adjust the bed thickness to account for changes in suspended sediment mass resulting from the updates. It might be possible to do this, but determining how such changes are distributed spatially is problematic. Figure 9 shows the time series of calculated total suspended mass for the pure model as well as for the direct insertion and kriging assimilation schemes. We see that the assimilation process does have the effect of adding suspended sediment to the system, but that the deviation in suspended

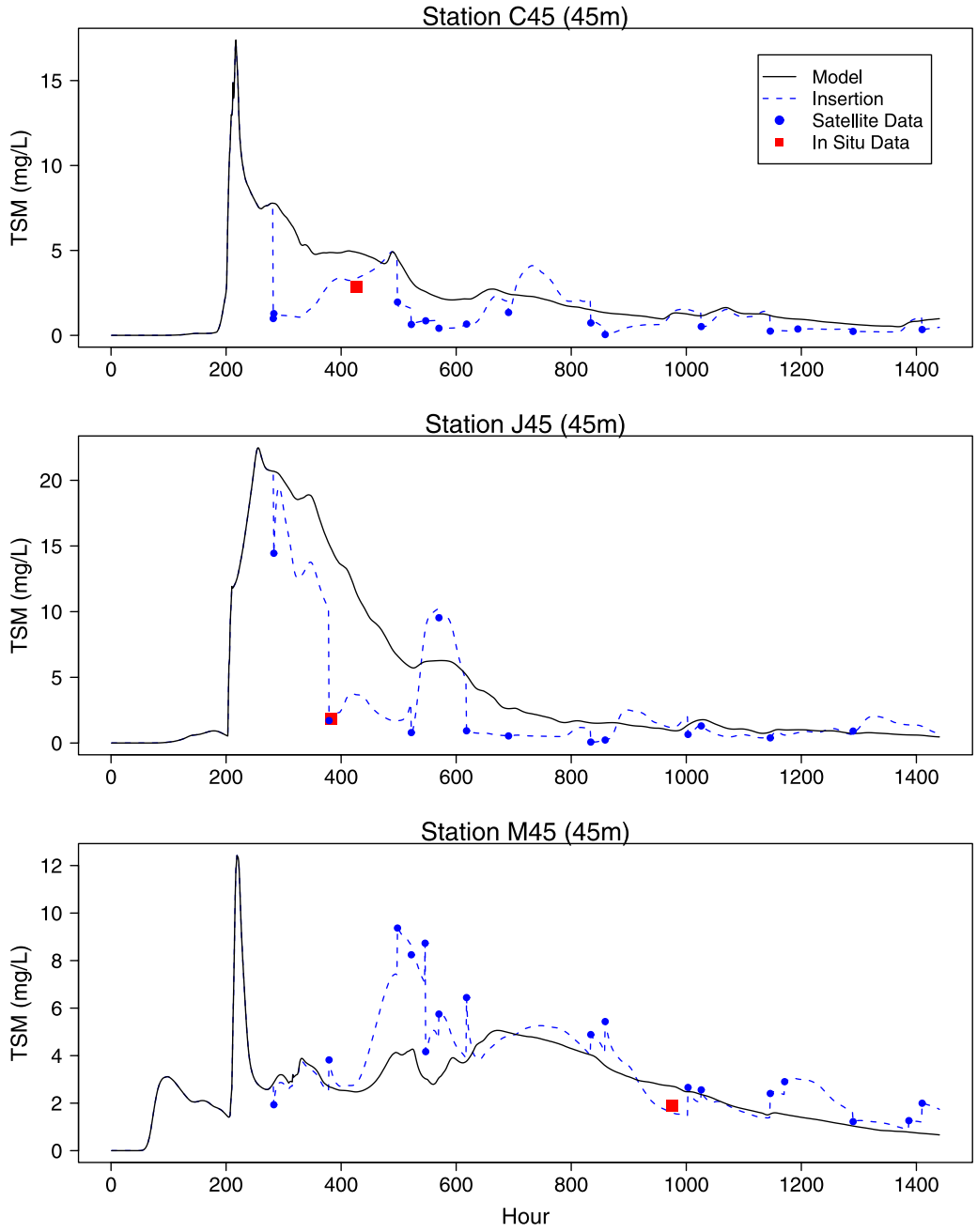

Figure 7. Time series of pure model and direct insertion forecasts at three locations in southern Lake Michigan (see Figure 1). Also plotted are the satellite data and the in situ measurements.

mass relative to the pure model (which is mass conservative) is small.

6. Conclusion

[59] This paper reports a study of forecasting sediment concentrations in Lake Michigan by combining a 2-D sediment transport model with SeaWiFS satellite images. We considered a number of different forecasting methods, including a purely data-based persistence approach, a purely physical model approach, and direct insertion and kriging data assimilation schemes which combine the model and satellite data sequentially. For each approach, we computed out-of-sample forecast RMSE and found that the direct insertion and kriging approaches improve forecast performance by 20% over the persistence approach and by 40% over the pure model results.

[60] We demonstrated that incorporating a time series of satellite images into a simple sediment transport model substantially improves forecasts of sediment concentrations in southern Lake Michigan. We believe that these methods can be applied in other coastal regions where modeling and forecasting of sediment transport are of interest. There are other possible applications of the approach including prediction of ice movement in coastal waters. Data availability need not necessarily be a limitation. Although we limited our original set of satellite images to reduce the effects of cloud contamination, we still had 20 good images spanning

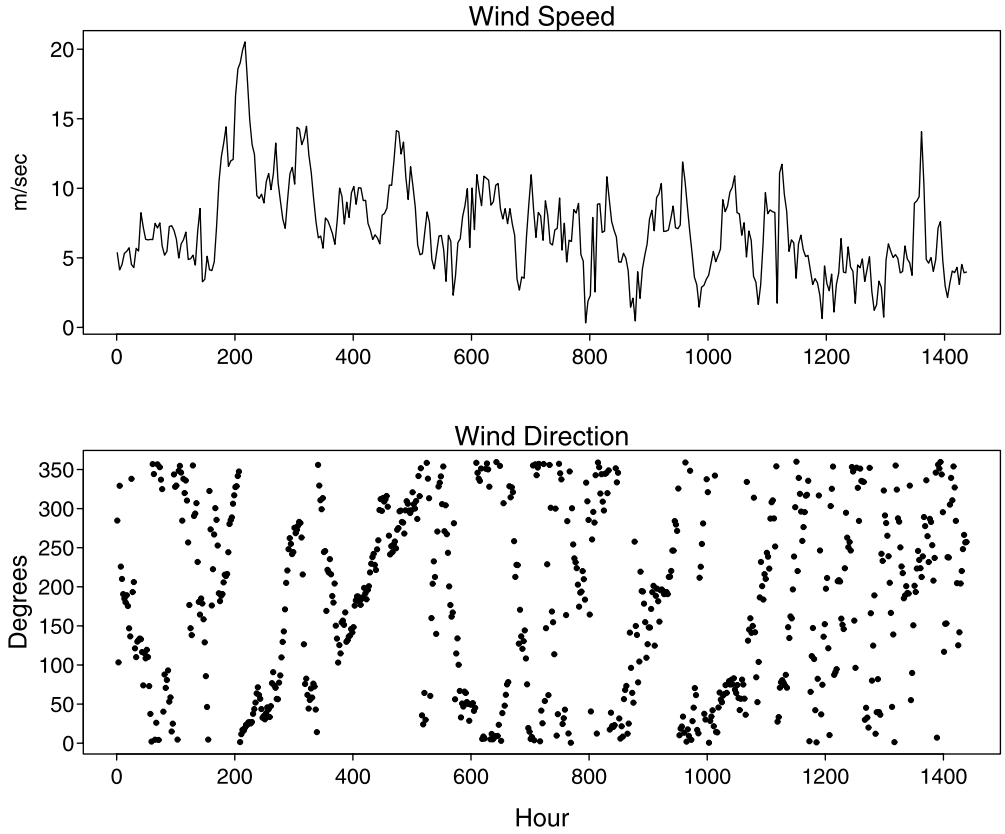

Figure 8. Time series of wind speed and direction in the center of northern Lake Michigan.

the 60-day study period, with an average of 5400 southern basin pixels each with which to work. This level of temporal and spatial data density would not be available from any other source.

[61] A number of future research directions remain. First, we plan to incorporate other sources of data into the assimilation scheme, including the in situ TSM measurements and the fluorescence data from the phytoplankton survey system (PSS). We also have available high-frequency time series of water currents at 11 locations in the southern basin of the lake, and these could be used to update the hydrodynamic model. Recently, *Zhang et al.* [2007] have shown that assimilating these current measurements significantly improves the advection fields, and it is likely that the improved advections will result in better prediction of suspended sediment. In a further step, the satellite, in situ, PSS, and current meter data could be used in a combined data assimilation scheme with a coupled hydrodynamic-sediment transport model. When sufficient in situ data are available, relaxation of the assumption that

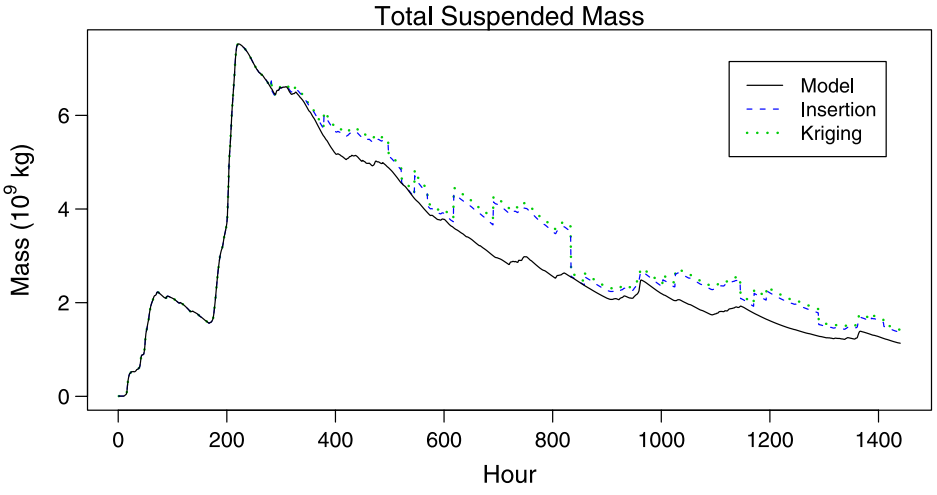

Figure 9. Time series of total suspended mass for the pure model, direct insertion and kriging approaches. Total mass is computed over the entire lake (14,458 pixels).

the sediment bed thickness and erosional properties are spatially uniform also would likely improve the model performance.

[62] Second, the methods used here could be extended to incorporate sequential parameter estimation for both the sediment transport model and the kriging covariance model. For the results reported here, the physical model and covariance parameters were chosen to minimize forecast RMSE. However, more formal statistical estimation procedures such as maximum likelihood and Bayesian methods would be preferable as they account for the spatial correlation in the errors. A third extension would be to provide retrospective (smoothed) estimates of the space-time trajectory of sediment concentrations given the full set of images. In contrast to the sequential methods described here, this would produce sediment fields without jumps at the observation times. A final extension would be to provide uncertainty estimates to accompany the concentration fields. We are currently developing methods based on the ensemble Kalman filter [*Evensen*, 1994] to generate realistic uncertainty fields.

Appendix A: Variational Approach for Kriging

[63] The kriging equation (9) can be written as

$$\mathbf{y}^u = \mathbf{y}^f + \mathbf{\Sigma H}'\mathbf{Q}^{-1}\mathbf{e},$$

where $\mathbf{e} = \mathbf{y}^o - \mathbf{H}\mathbf{y}^f$ is the $m \times 1$ forecast error vector and $\mathbf{Q} = \mathbf{H\Sigma H}'$ is the $m \times m$ forecast covariance matrix defined at the cloud-free locations. The update is implemented in three steps: (1) Solve $\mathbf{Qz} = \mathbf{e}$. (2) Compute $\mathbf{w} = \mathbf{\Sigma H}'\mathbf{z}$. (3) Compute $\mathbf{y}^u = \mathbf{y}^f + \mathbf{w}$. The last two steps are straightforward as step 2 involves a sparse matrix-vector multiplication and step 3 requires addition of two vectors. Step 1 is more computationally intensive as it requires solving a system of order m, the dimension of the observation. To solve the system, we rely on a variational approach in which $\mathbf{z}$ is defined as the minimizer of the function

$$f(\mathbf{z}) = \frac{1}{2}\mathbf{z}'\mathbf{Qz} - \mathbf{z}'\mathbf{e}.$$

We use an efficient preconditioned conjugate gradient (CG) algorithm [*Golub and Van Loan*, 1996] to perform the minimization. The CG requires only vector-vector multiplications and matrix-vector products of the form $\mathbf{Qz}$. Because of our assumption of a compactly supported covariance function, $\mathbf{Q}$ is sparse and the matrix-vector products can be computed efficiently using sparse matrix routines. Using a convergence tolerance of 10^{-5} and a starting value of $\mathbf{z} = \mathbf{0}$, we find that the algorithm typically converges within 25 iterations (less than 5 s of CPU time) for each image update.

[64] **Acknowledgments.** We thank the SeaWiFS Project and the Ocean Color Data Archive at the Goddard Space Flight Center for the production and distribution of the SeaWiFS data respectively. We also thank the EEGLE Project for collection and distribution of the in situ data used here. NOAA's Coastal Ocean Program supported work at ANL and GLERL, originally as part of EEGLE. Subsequent funding was provided by the U.S. Environmental Protection Agency (EPA) through Science To Achieve Results (STAR) Cooperative Agreement R-82940201 to the University of Chicago for the Center for Integrating Statistical and Environmental Science (CISES). However, this research has not been subjected to the EPA's required peer and policy review and therefore does not necessarily reflect the views of the Agency, and no official endorsement should be inferred. This is GLERL contribution 1491.

References

Baith, K., R. Lindsay, G. Fu, and C. R. McClain (2001), Data analysis system developed for ocean color satellite sensors, *Eos Trans. AGU*, *82*(18), 202.

Behrenfeld, M. J., et al. (2001), Biospheric primary production during an ENSO transition, *Science*, *291*(5513), 2594–2597.

Beletsky, D., and D. J. Schwab (2001), Modeling circulation and thermal structure in Lake Michigan: Annual cycle and interannual variablility, *J. Geophys. Res.*, *106*(C9), 19,745–19,771.

Beletsky, D., J. H. Saylor, and D. J. Schwab (1999), Mean circulation in the Great Lakes, *J. Great Lakes Res.*, *25*, 78–93.

Beletsky, D., D. J. Schwab, P. J. Roebber, M. J. McCormick, G. S. Miller, and J. H. Saylor (2003), Modeling wind-driven circulation during the March 1998 sediment resuspension event in Lake Michigan, *J. Geophys. Res.*, *108*(C2), 3038, doi:10.1029/2001JC001159.

Binding, C. E., D. G. Bowers, and E. G. Mitchelson-Jacob (2003), An algorithm for the retrieval of suspended sediment concentrations in the Irish Sea from SeaWiFS ocean colour satellite imagery, *Int. J. Remote Sens.*, *24*, 3791–3806.

Binding, C. E., D. G. Bowers, and E. G. Mitchelson-Jacob (2005), Estimating suspended sediment concentrations from ocean colour measurements in moderately turbid waters; the impact of variable particle scattering properties., *Remote Sens. Environ.t*, *94*(3), 373–383.

Brock, J. C., and C. R. McClain (1992), Interannual variability in phytoplankton blooms observed in the northwestern Arabian Sea during the southwest monsoon, *J. Geophys. Res.*, *97*(C1), 733–750.

Budd, J. W., and D. S. Warrington (2004), Satellite-based sediment and chlorophyll a estimates for Lake Superior, *Journal of Great Lakes Research– Special Issue on Lake Superior*, *30*(0), 459–466.

Cardenas, M. P., D. J. Schwab, B. Eadie, N. Hawley, and B. M. Lesht (2005), Sediment transport model validation in Lake Michigan, *J. Great Lakes*, *31*.

Chapra, S. C. (1977), Total phosphorus model for the Great Lakes, *J. Environ. Eng. Div. Am. Soc. Civ. Eng.*, *103*(EE2), 147–161.

Chen, C., L. Wang, R. Ji, J. W. Budd, D. J. Schwab, D. Beletsky, G. L. Fahnenstiel, H. Vanderploeg, B. Eadie, and J. Cotner (2004), Impacts of suspended sediment on the ecosystem in Lake Michigan: A comparison between the 1998 and 1999 plume events, *J. Geophys. Res.*, *109*, C10S05, doi:10.1029/2002JC001687.

Cressie, N. A. C. (1993), *Statistics for Spatial Data*, rev. ed., John Wiley, New York.

Eadie, B. J., et al. (1996), Anatomy of a recurrent episodic event: A winter-spring plume southern Lake Michigan, *Eos Trans. AGU*, *77*, 337–338.

Eadie, B. J., et al. (2002), Particle transport, nutrient cycling and algal community structure associated with a major winter-spring sediment resuspension event in southern Lake Michigan, *J. Great Lakes Res.*, *28*(3), 324–337.

Evensen, G. (1994), Sequential data assimilation with a nonlinear quasi-geostrophic model using Monte-Carlo methods to forecast error statistics, *J. Geophys. Res.*, *99*(5), 10,143–10,162.

Gaspari, G., and S. Cohn (1999), Construction of correlation functions in two and three dimensions, *Q. J. R. Meteorol. Soc.*, *125*, 723–757.

Gerritsen, H., J. G. Boon, T. van der Kaaij, and R. J. Vos (2001), Integrated modelling of suspended matter in the North Sea, *Estuarine Coastal Shelf Sci.*, *53*, 581–594.

Golub, G. H., and C. F. Van Loan (1996), *Matrix Computations*, Johns Hopkins Press, Baltimore, Md.

Gordon, H. R., and M. Wang (1994), Retrieval of water-leaving radiance and aerosol optical thickness over the oceans with SeaWiFS: A preliminary algorithm, *Appl. Opt.*, *33*, 443–452.

Hawley, N., and C.-H. Lee (1999), Sediment resuspension and transport in Lake Michigan during the unstratified period, *Sedimentology*, *46*, 791–805.

Hawley, N., and B. M. Lesht (1992), Sediment resuspension in Lake St. Clair, *Limnol. Oceanogr.*, *37*(8), 1720–1737.

Hawley, N., and R. W. Muzzi (2003), Observations of nephelopid layers made with an autonomous vertical profiler, *J. Great Lakes Res.*, *29*(1), 124–133.

Hughes, C. W., M. S. Jones, and S. Carnochan (1998), Use of transient features to identify eastward currents in the Southern Ocean, *J. Geophys. Res.*, *103*(C2), 2929–2943.

Kalnay, E. (2003), *Atmospheric Modeling, Data Assimilation, and Predictability*, 341 pp., Cambridge Univ. Press, New York.

Kostinoy, A. G., A. I. Ginzburg, M. Frankingoulle, and B. Delille (2004), Fronts in the southern Indian Ocean as inferred from satellite sea surface temperature data, *J. Mar. Syst.*, *45*(1–2), 55–73.

Krone, R. B. (1962), Flume studies of the transport of sediment in estuarial shoaling processes, technical report, Hydraul. Eng. Lab. and Sanit. Eng. Res. Lab., Univ. of Calif., Berkeley.

Lee, C., D. J. Schwab, and N. Hawley (2005), Sensitivity analysis of sediment resuspension parameters in coastal area of southern Lake Michigan, *J. Geophys. Res.*, *110*, C03004, doi:10.1029/2004JC002326.

Lee, C., D. J. Schwab, D. Beletsky, J. Stroud, and B. Lesht (2007), Numerical modeling of mixed sediment resuspension, transport, and deposition during the March 1998 episodic events in southern Lake Michigan, *J. Geophys. Res.*, *112*, C02018, doi:10.1029/2005JC003419.

Lesht, B. M. (1989), Climatology of sediment transport on Indiana Shoals, Lake Michigan, *J. Great Lakes Res.*, *15*, 486–497.

Lesht, B. M., and N. Hawley (1987), Near-bottom currents and suspended sediment concentration in southeastern Lake Michigan, *J. Great Lakes Res.*, *13*, 375–386.

Lesht, B. M., T. D. Fontaine, and D. M. Dolan (1991), Great-lakes total phosphorus model—Post audit and regionalized sensitivity analysis, *J. Great Lakes Res.*, *17*(1), 3–17.

Lesht, B. M., J. R. Stroud, M. J. McCormick, G. L. Fahnenstiel, M. L. Stein, L. J. Welty, and G. A. Leshkevich (2002), An event-driven phytoplankton bloom in southern Lake Michigan observed by satellite, *Geophys. Res. Lett.*, *29*(8), 1177, doi:10.1029/2001GL013533.

Liebig, J. R., H. A. Vanderploeg, and S. A. Ruberg (2006), Factors affecting the performance of the optical plankton counter in large lakes: Insights from Lake Michigan and laboratory studies, *J. Geophys. Res.*, *111*, C05S02, doi:10.1029/2005JC003087.

Mitchelson-Jacob, E. G. (1999), Retrieval of suspended particulate matter concentrations from ocean colour imagery, *Tech. Rep. UCES Report U99-2, Document DP-CSM/1099-004*, Unit for Coastal and Estuarine Stud., Univ. of Wales, Bangor, U.K.

Mortimer, C. H. (1988), Discoveries and testable hypotheses arising from coastal zone color scanner imagery of southern Lake Michigan, *Limnol. Oceanogr.*, *33*(2), 203–226.

Myint, S. W., and N. Walker (2002), Quantification of surface suspended sediments along a river dominated coast with NOAA AVHRR and SeaWiFS measurements: Louisiana, USA, *Int. J. Remote Sens.g*, *23*(16), 3229–3249.

Ouillon, S., P. Douillet, and S. Andréfouët (2004), Coupling satellite data with in situ measurements and numerical modeling to study fine suspended-sediment transport: A study for the lagoon of New Caledonia, *Coral Reefs*, *23*, 109–122, doi:10.1007/s000338-003-0352-z.

Partheniades, E. (1962), A study of erosion and deposition of cohesive soils in salt water, Ph.D. thesis, Univ. of Calif., Berkeley.

Pleskachevsky, A., G. Gayer, J. Horstmann, and W. Rosenthal (2005), Synergy of satellite remote sensing and numerical modeling for monitoring of suspended particulate matter, *Ocean Dyn.*, *55*, 2–9, doi:10.1007/s10236-004-0101-z.

Puls, W., R. Doerffer, and J. Sündermann (1994), Numerical simulation and satellite observations of suspended matter in the North Sea, *IEEE J. Oceanic Eng.*, *19*(1), 3–9, doi:10.1109/48.289444.

Ransibrahmanakul, V., and R. P. Stumpf (2002), The use of AVHRR satellite data for estimating spatially varying critical wind stress in Florida Bay, *J. Coastal Res.*, *18*(2), 267–273.

Rao, Y. R., C. R. Murthy, M. J. McCormick, G. S. Miller, and J. H. Saylor (2002), Observations of circulation and coastal exchange characteristics in southern Lake Michigan during 2000 winter season, *Geophys. Res. Lett.*, *29*(13), 1631, doi:10.1029/2002GL014895.

Schwab, D. J., and K. W. Bedford (1994), Initial implementation of the Great Lakes Forecasting System: A real-time system for predicting lake circulation and thermal structure, *Water Pollut. Res. J. Can.*, *29*, 203–220.

Schwab, D. J., and D. Beletsky (2002), Hydrodynamic and sediment transport modeling of episodic resuspension events in Lake Michigan, in *Proceedings of the Seventh International Conference on Estuarine and Coastal Modeling*, edited by M. Spaulding, pp. 266–279, A. Soc. of Civ. Eng., Reston, Va.

Schwab, D. J., J. R. Bennett, P. C. Liu, and M. A. Donelan (1984), Application of a simple numerical wave prediction model to Lake Erie, *J. Geophys. Res.*, *89*(C3), 3586–3589.

Schwab, D. J., D. Beletsky, and J. Lou (2000), The 1998 coastal turbidity plume in Lake Michigan, *Estuarine, Coastal and Shelf Science*, *50*, 49–58.

Stein, M. L. (1999), *Interpolation of Spatial Data: Some Theory for Kriging*, Springer, New York.

Uddstrom, M. J., and N. A. Oien (1999), On the use of high-resolution satellite data to describe the spatial and temporal variability of sea surface temperatures in the New Zealand region, *J. Geophys. Res.*, *104*(C9), 20,729–20,751.

Warrick, J. A., L. A. K. Mertes, D. A. Siegel, and C. Mackenzie (2004), Estimating suspended sediment concentrations in turbid coastal waters of the Santa Barbara Channel with SeaWiFS, *Int. J. Remote Sens.*, *25*(10), 1995–2002.

Winkleman, A. G., E. R. Stabenau, and B. J. Eadie (1998), Particle distribution and concentration of total suspended matter in southern Lake Michigan, *NOAA Tech. Memo ERL GLERL-105*, Great Lakes Environ. Res. Lab., Ann Arbor, Mich.

Zhang, Z., D. Beletsky, D. J. Schwab, and M. L. Stein (2007), Assimilation of current measurements into a circulation model of Lake Michigan, *Water Resour. Res.*, *43*, W11407, doi:10.1029/2006WR005818.

D. Beletsky, CILER, SNRE, University of Michigan, 2205 Commonwealth Boulevard, Ann Arbor, MI 48105, USA. (dima.beletsky@noaa.gov)

B. M. Lesht, Applied Science and Technology Directorate, Argonne National Laboratory, 9700 South Cass Avenue, Argonne, IL 60439, USA. (bmlesht@anl.gov)

D. J. Schwab, NOAA/GLERL, 2205 Commonwealth Boulevard, Ann Arbor, MI 48105, USA. (david.schwab@noaa.gov)

M. L. Stein, Department of Statistics, University of Chicago, 5734 South University Avenue, Chicago, IL 60637, USA. (stein@galton.uchicago.edu)

J. R. Stroud, Department of Statistics, George Washington University, 2140 Pennsylvania Avenue, N.W., Washington, DC 20052, USA. (stroud@gwu.edu)